

# 1 Measurement of the Earth tides with a MEMS gravimeter

2 R. P. Middlemiss,<sup>\* †</sup> A. Samarelli,<sup>\*</sup> D. J. Paul,<sup>†</sup> J. Hough,<sup>\*</sup> S. Rowan<sup>\*</sup> and G. D. Hammond<sup>\*</sup>

3 The ability to measure tiny variations in the local gravitational acceleration allows – amongst  
4 other applications – the detection of hidden hydrocarbon reserves, magma build-up before volcanic  
5 eruptions, and subterranean tunnels. Several technologies are available that achieve the sensi-  
6 tivities required for such applications (tens of  $\mu\text{Gal}/\sqrt{Hz}$ ): free-fall gravimeters<sup>1</sup>, spring-based  
7 gravimeters<sup>2,3</sup>, superconducting gravimeters<sup>4</sup>, and atom interferometers<sup>5</sup>. All of these devices can  
8 observe the Earth Tides<sup>6</sup>; the elastic deformation of the Earth’s crust as a result of tidal forces.  
9 This is a universally predictable gravitational signal that requires both high sensitivity and high  
10 stability over timescales of several days to measure. All present gravimeters, however, have limita-  
11 tions of excessive cost ( $> \$100$  k) and high mass ( $>8$  kg). We have built a microelectromechanical  
12 system (MEMS) gravimeter with a sensitivity of  $40 \mu\text{Gal}/\sqrt{Hz}$  in a package size of only a few  
13 cubic centimetres. We demonstrate the remarkable stability and sensitivity of our device with a  
14 measurement of the Earth tides. Such a measurement has never been undertaken with a MEMS  
15 device, and proves the long term stability of our instrument compared to any other MEMS device,  
16 making it the first MEMS accelerometer to transition from seismometer to gravimeter. This heralds  
17 a transformative step in MEMS accelerometer technology. MEMS accelerometers – found in most  
18 smart phones<sup>7</sup> – can be mass-produced remarkably cheaply, but most are not sensitive enough,

---

<sup>\*</sup>S.U.P.A., University of Glasgow, School of Physics and Astronomy, Kelvin Building, University Avenue, Glas-  
gow, G12 8QQ, U.K.

<sup>†</sup>University of Glasgow, School of Engineering, Rankine Building, Oakfield Avenue, Glasgow, G12 8LT, U.K.

19 and none have been stable enough to be called a ‘gravimeter’. Due to their small size and low cost,  
20 MEMS gravimeters could create a new paradigm in gravity mapping: exploration surveys could  
21 be carried out with drones instead of low-flying aircraft; they could be used for distributed land  
22 surveys in exploration settings, for the monitoring of volcanoes; or built into multi-pixel density  
23 contrast imaging arrays.

24 Gravimeters can be split into two broad categories: absolute gravimeters and relative gravime-  
25 ters. Absolute gravimeters measure the gravitational acceleration,  $g$ , by timing a mass in free  
26 fall over a set distance. Absolute gravimeters are very accurate but are bulky and expensive.  
27 The *Micro-g Lacoste FG5*<sup>1</sup>, for example, achieves acceleration sensitivities of  $1.6 \mu\text{Gal}/\sqrt{Hz}$   
28 ( $1.6 \mu\text{Gal}/\sqrt{Hz}$  is an acceleration measurement of  $1.6 \mu\text{Gal}$  in an integration time of 1 second,  
29 where 1 Gal is  $1 \text{ cm/s}^2$ ), but it costs over \$100 k and weighs 150 kg. Relative gravimeters make  
30 gravity measurements relative to the extension of a spring: the deflection of a mass on a spring  
31 will change as  $g$  varies. These devices can be made smaller than absolute gravimeters but are in-  
32 trinsically less stable: the spring constant can change with varying environmental conditions. The  
33 *Scintrex CG5* relative gravimeter (also costing over \$100 k, but weighing 8 kg) can measure gravity  
34 variations down to  $2 \mu\text{Gal}^{2,3}$  but is much more susceptible to drift than absolute devices. For any  
35 mass-on-spring system, increased acceleration sensitivity is achieved by either improving the sen-  
36 sitivity to displacement, or by minimising the ratio,  $k/m$ , between the spring constant,  $k$ , and the  
37 mass,  $m$ . A system in which a mass is suspended from a spring within a rigid housing will respond  
38 differently to signals above or below the resonance frequency. In the regime below the resonance  
39 there will be a linear relationship between the displacement of the proof mass and the acceleration  
40 of the housing. This is the region in which the device can be used as an accelerometer/gravimeter.

41 MEMS devices are microscopic mechanical devices made from semiconductor materials. They  
42 have the advantage of being mass-producible, light-weight and cheap. Although mobile phone

43 accelerometers are not very sensitive, some MEMS devices have been developed that reach sensi-  
44 tivities much better than the  $0.23 \text{ mGal}/\sqrt{\text{Hz}}$  of the iPhone MEMS device<sup>7</sup>. For example: a device  
45 developed by Krishnamoorthy et. al.<sup>8</sup> has a sensitivity of  $17 \text{ }\mu\text{Gal}/\sqrt{\text{Hz}}$ ; the *SERCEL QuietSieis*<sup>9</sup>  
46 has a sensitivity of  $15 \text{ }\mu\text{Gal}/\sqrt{\text{Hz}}$ ; and a microseismometer developed by Pike et. al.<sup>10</sup> has a sensi-  
47 tivity of  $2 \text{ }\mu\text{Gal}/\sqrt{\text{Hz}}$ . These devices, however, can only operate as seismometers and do not have  
48 a stability sufficient to be classed as gravimeters, which are capable of monitoring low frequency  
49 gravimetric signals such as the Earth tides (around  $10 \text{ }\mu\text{Hz}$ ). Table 1 summarises the characteristics  
50 of these MEMS seismometers, the *Scintrex CG5* gravimeter, and our own gravimeter. Figure 11  
51 provides a further comparison between our own device, the Pike microseismometer<sup>10</sup>, the *Scintrex*  
52 *CG5* and two other commercial devices.

53 The Earth tides are an elastic deformation of the Earth's crust caused by the changing rel-  
54 ative phase of the Sun, the Earth and the Moon<sup>6</sup>. They produce a small variation in the local  
55 gravitational acceleration, the size of which depends also on the latitude and elevation of the mea-  
56 surement location. Depending on the time of the lunar month, the Earth tides vary in amplitude  
57 and frequency, moving between diurnal ( $2 \times 10^{-5} \text{ Hz}$ ) and semi-diurnal ( $1 \times 10^{-5} \text{ Hz}$ ) peaks. Since  
58 the Earth tides have a peak signal strength<sup>3</sup> of less than  $400 \text{ }\mu\text{Gal}$ , and a low frequency oscillation,  
59 they are a useful natural signal to demonstrate both the sensitivity and long-term stability of any  
60 gravimeter. The Earth tides have never previously been measured with any MEMS device, so a  
61 device able to do so will be a transformative step change in the field.

62 Our device has been designed to have a resonant frequency of under  $4 \text{ Hz}$ . To achieve such  
63 low frequencies a geometric anti-spring system<sup>11,12</sup> was chosen. With increasing displacement,  
64 anti-springs get softer and their resonant frequency gets lower. A geometrical anti-spring requires  
65 a pair of arched flexures that meet at a constrained central point. In the case of our MEMS device  
66 they meet at the proof mass. This geometry constrains the motion of the proof mass to the axis

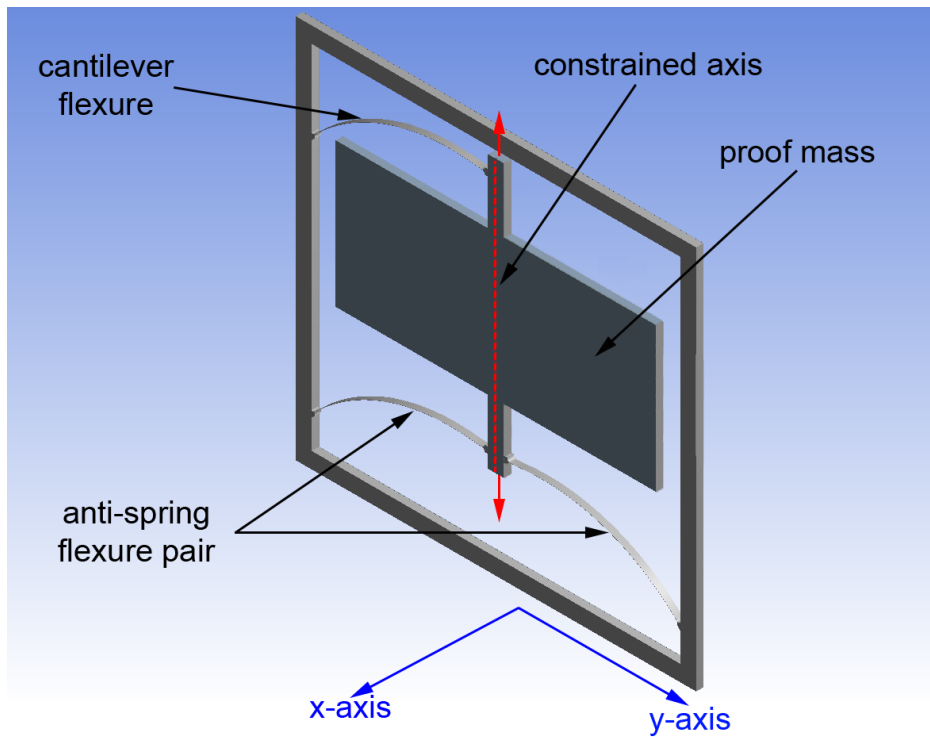


Figure 1

67 shown in Fig. 1. As the proof mass is pulled away from its un-loaded position the spring constant is  
 68 lowered. This is in contrast to a Hooke's-law spring, in which the spring constant does not change  
 69 with increasing displacement. Tilting the MEMS device from horizontal to vertical orientation,  
 70 pulls the proof mass down, thus lowering the frequency from over 20 Hz when horizontal to 2.3 Hz  
 71 when vertical. We have opted for a configuration with a pair of anti-spring flexures supporting the  
 72 lower portion of the proof mass, and a single flexure supporting the top. All of the flexures are  
 73 only  $5 \mu\text{m}$  wide but  $200 \mu\text{m}$  deep. The three flexure system maintains an anti-spring behaviour  
 74 as the gravitational loading increases (when the device is tilted from horizontal to vertical). Due  
 75 to the asymmetry of the design, however, a small level of y-axis tilting occurs. This tilt pulls the  
 76 system off its constrained axis. When the system reaches its equilibrium, it gains a Hooke's Law  
 77 behaviour (see methods section and Fig. 5 for further details). We thus have a device which is  
 78 stable but at a much lower frequency than traditional MEMS devices. A resonant frequency of

79 2.3 Hz is the lowest resonant frequency of any reported MEMS device to date. To our knowledge  
80 the next lowest resonant frequency reported is 10.2 Hz in a device made by Pike et al.<sup>13</sup>. The  
81 fact that the system has a Hooke’s law behaviour in its vertical configuration means that it is  
82 less sensitive to tilt in the x-axis (see Fig. 1) than would be the case for a normal geometrical  
83 anti-spring (see Fig. 12).

84 The proof mass motion is measured using an optical shadow sensor<sup>14</sup>. Here a light emitting  
85 diode (LED) illuminates a photodiode with the MEMS device mounted in between. Motion of the  
86 proof mass modulates the shadow, generating a change in the current output of the photodiode.  
87 This shadow sensor (Fig. 2) achieves a high sensitivity (equating to an acceleration noise floor of  
88  $\leq 10 \mu Gal$  at the sampling frequency of 0.03 Hz), whilst allowing a large dynamic range of up to  
89  $50 \mu m$ .

90 Observation of the Earth tides requires stable operation over several days. The main contribu-  
91 tor to parasitic motion is the varying temperatures of the system. For this reason the ‘C’-shaped  
92 structure of the shadow sensor was fabricated from fused silica because of its low thermal expan-  
93 sion coefficient at room temperature ( $4.1 \times 10^{-7} K^{-1}$ )<sup>15</sup>. Silicon has a significantly larger thermal  
94 expansion coefficient ( $2.6 \times 10^{-6} K^{-1}$ )<sup>16</sup>, but silicon was used to make the MEMS because it is  
95 a standard fabrication material in the semiconductor industry, it has high mechanical strength,  
96 and its thermal properties are well characterised. The dominant mechanism by which temperature  
97 variations affect the gravity measurement is the change in Young’s modulus,  $Y$ , of the flexures<sup>17, 18</sup>.  
98 This in turn alters the spring constant of the flexures, resulting in a variation of  $k$ ,  $1/k dk/dT$ ,  
99 of  $7.88 \times 10^{-6} K^{-1}$ . We therefore implemented servo control loops to maintain the temperature  
100 of the system to within 1 mK. A 1 mK change in temperature would give an uncertainty in the  
101 gravity reading of  $\sim 25 \mu Gal$ . The primary control loop maintained the temperature of the MEMS  
102 device directly, the second controlling the temperature of a copper thermal shield that encased the

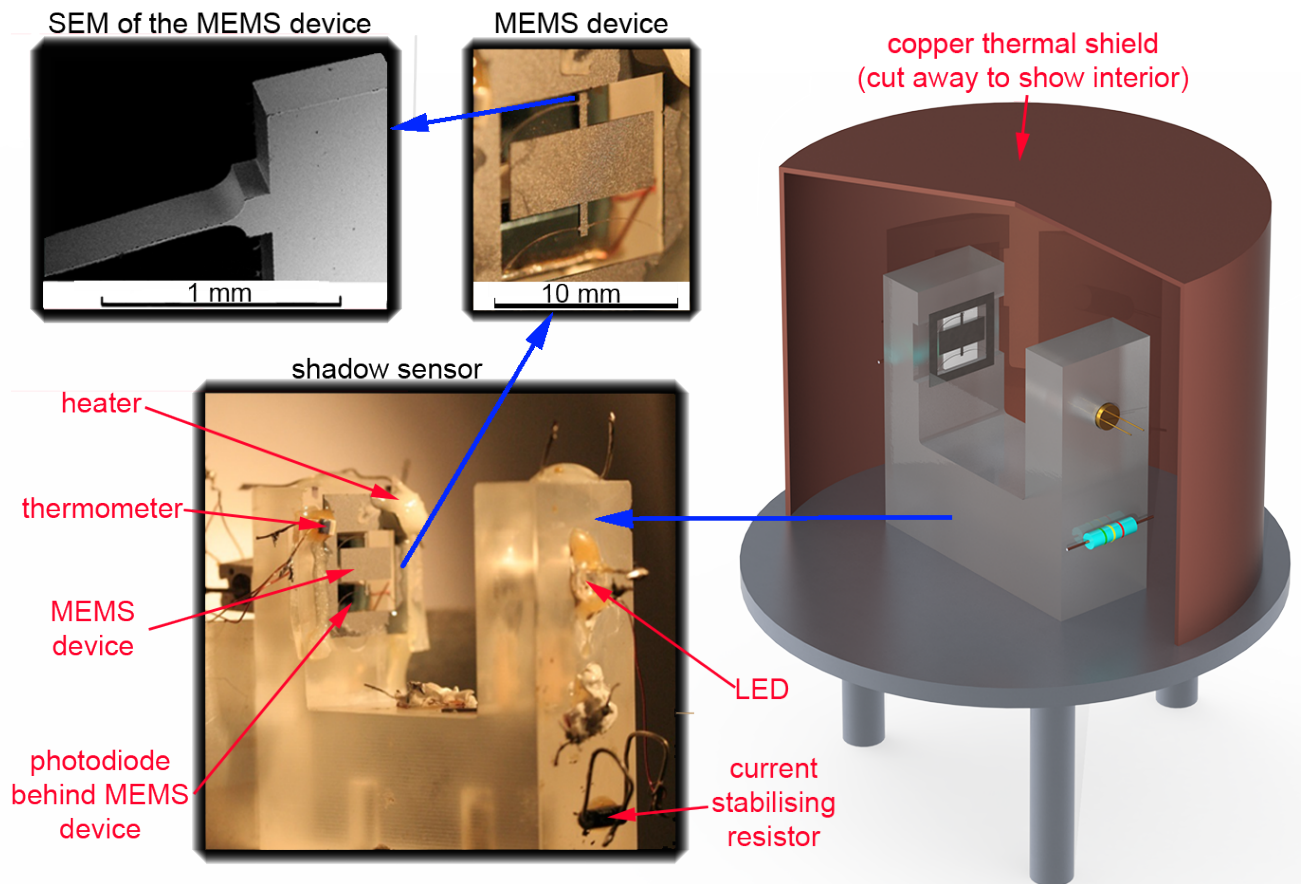


Figure 2

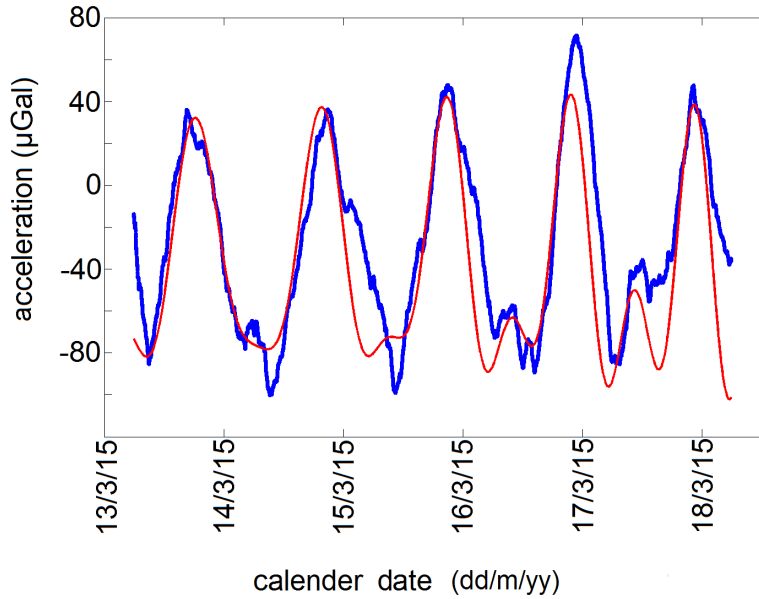


Figure 3

103 entire shadow sensor (Fig. 2). The MEMS device was placed inside a vacuum system. This was  
 104 bolted to the floor without an external seismic isolation table, which would be a large  
 105 and expensive addition.

106 From December 2014 the system was left in continuous operation whilst the servo control was  
 107 optimised. Figure 3 demonstrates a data run of five days between the 13/03/15 to the 18/03/15  
 108 in which gravitational acceleration is plotted against time. The blue data demonstrates our exper-  
 109 imental data averaged with a time constant of 240 minutes (the full noise data can be observed  
 110 in Fig. 6a), together with a data set filtered with a 10 minute time constant (Fig. 6b). The solid  
 111 red line is a theoretical plot of the Earth tides as should be observed at our location ( $55.8719^\circ$  N,  
 112  $4.2875^\circ$  W), and was plotted using *TSOFT*<sup>19</sup>. An ocean loading correction is also included in  
 113 this theoretical plot to account for the effect of nearby tidal waters pressing on the Earth's crust,  
 114 although the effect is at the level of 5% for our laboratory. There is a strong correlation coefficient,  
 115  $R$ , of 0.86 between our experimental data and the theory plot. The correlation indicates that  
 116 this is the first measurement of Earth tides demonstrated by a MEMS device, a landmark result

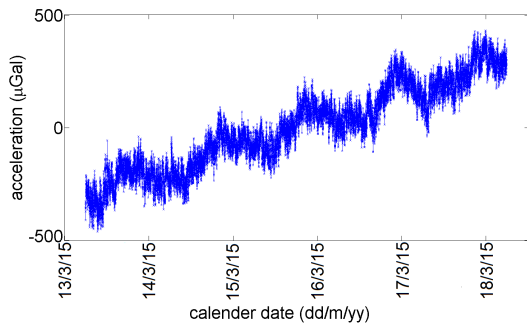
117 for MEMS gravimetry. This measurement provides a natural calibration for the gravimeter, the  
118 results of which allow us to determine that the present sensitivity of the device is  $40 \mu\text{Gal}/\sqrt{\text{Hz}}$ .  
119 We further performed a stability test of the calibration factor for our device by monitoring the  
120 tides at two intervals approximately 3 months apart. The calibration remained constant to better  
121 than 5 % (Fig. 13).

122 The noise floor of our device is limited by seismic noise. A theoretical thermal noise floor of  
123 under  $0.5 \mu \text{Gal}/\sqrt{\text{Hz}}$  can be calculated, assuming that losses are due to structural damping<sup>20</sup>.  
124 This calculation is based upon a measurement of the quality factor,  $Q$ , of the device under vacuum  
125 of  $\sim 80$  (the relaxation time of the MEMS device is  $\sim 11$  s). We observe that the  $Q$  reduces as the  
126 resonant frequency is lowered (Fig. 7). This behaviour is due to the fact that in geometrical anti-  
127 springs: as the resonant frequency is lowered, the restoring force becomes comparable to internal  
128 friction<sup>21</sup>.

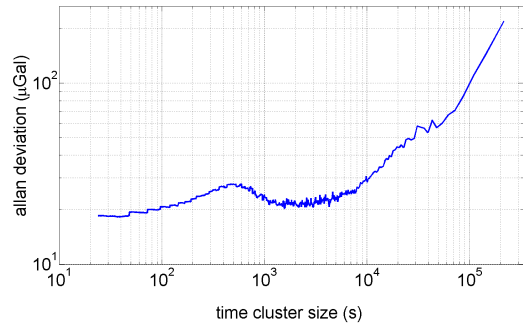
129 To put the sensitivity of our device into context,  $40 \mu\text{Gal}/\sqrt{\text{Hz}}$  is sufficient in 1 second to  
130 detect a tunnel with a cross-sectional area of  $2 \text{ m}^2$  and length of 4 m at a depth of 2 m; it could be  
131 used to find oil reservoirs of  $\geq 50 \text{ m} \times 50 \text{ m} \times 50 \text{ m}$  (with a density contrast of 50%) at a depth of  
132 150 m; a change of  $45 \mu\text{Gal}$  was a ‘clear precursor’ to a volcanic eruption in the Canary Islands in  
133 2011<sup>22</sup>. It is accepted that intrusion of new magma into a reservoir precedes volcanic eruptions<sup>23</sup>;  
134 continuous micro gravity measurements around volcanoes are a useful tool in monitoring such  
135 events<sup>24</sup>. The ratio of ground deformation to change in gravity can be used to monitor magma  
136 chambers at depths of several km<sup>25</sup>.

137 In figure 3 a linear drift term has been removed from the data. This drift equates to less than  
138  $150 \mu\text{Gal}$  per day, a factor of three better than the drift of the *Scintrex CG5* ( $500 \mu\text{Gal}$  per day).  
139 Both we and *Scintrex CG5* auto-correct this drift with software. Figure 4 consists of eight subplots  
140 demonstrating the drift characteristics on the MEMS device. Figure 4a shows the full-noise tide

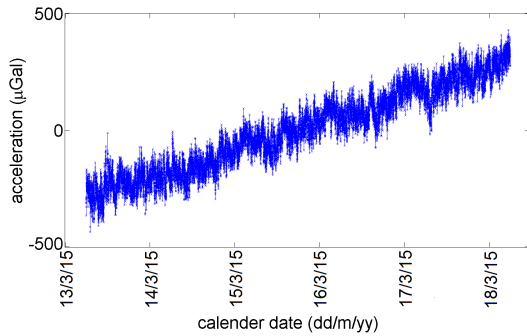




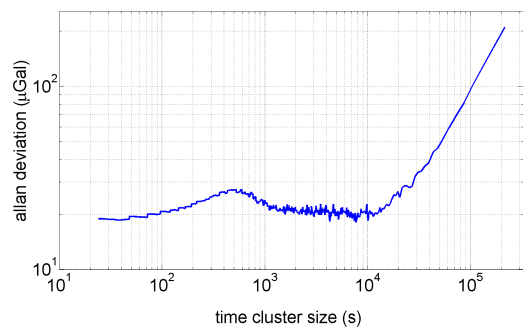
(a)



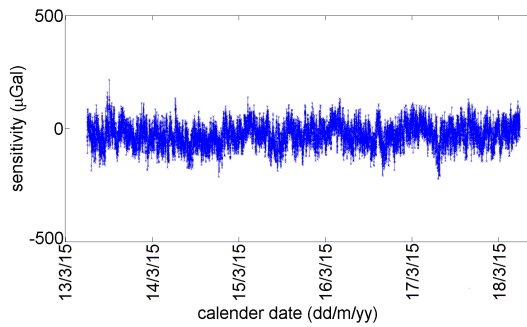
(b)



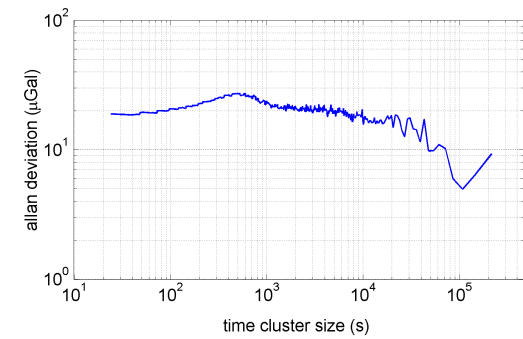
(c)



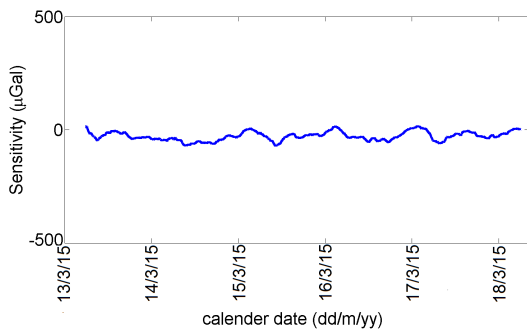
(d)



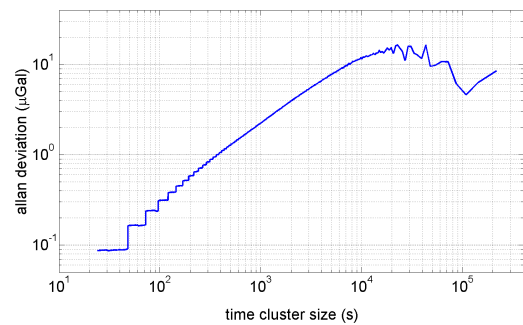
(e)



(f)



(g)



(h)

Figure 4

141 data without a linear drift correction. Figure 4c shows the same data but with the tide signal  
142 removed. Figure 4e shows the same data again but with a linear drift correction. Figures 4b, 4d,  
143 4f and 4h show the Allan deviation for the data in figures 4a, 4c, 4e and 4g respectively. Allan  
144 deviation is a technique used to measure the variation over the full frequency range of a signal by  
145 averaging over increasingly larger time intervals<sup>26</sup>.

146 The data analysed in figure 4 spans a frequency range from  $10^{-5}$  Hz to 0.03 Hz (the sampling  
147 frequency of this data set, which was used to remove the effect of seismic noise). A second data set  
148 was taken at a faster sampling rate to observe the response of the device from 0.03 Hz up to the  
149 resonant frequency of 2.3 Hz. Both data sets can be observed in figure 10 in the form of a RMS  
150 acceleration sensitivity plot. The Allan deviation for the high frequency series is polluted by the  
151 presence of two large signals: the resonant frequency of the device, and the microseismic peak<sup>27, 28</sup>.  
152 This deviation plot is not a useful measure of the noise of the device and has therefore not been  
153 included in figure 4. Figures 4b and 4d demonstrate the linear drift that the device experiences.  
154 Figures 4b, 4d and 4f also demonstrate a small peak at 500 s that is an artefact of the temperature  
155 servo. The broad peak that is only visible on the rising edge of Fig. 4b is the tide signal. A  
156 comparison between the drift characteristics of our device and some other commercial gravimeters  
157 is displayed in figure 11, in which an acceleration power spectral density plot is displayed.

158 This MEMS device, capable of measuring the Earth tides, represents a significant step forward  
159 in the field – it is not just an accelerometer, but a gravimeter. Made from a single silicon chip  
160 the size of a postage stamp, this sensor has the lowest reported resonant frequency of any MEMS  
161 accelerometer (2.3 Hz), is within an order of magnitude of the best acceleration sensitivity of any  
162 MEMS device ( $40 \mu Gal/\sqrt{Hz}$ ), and has the best reported stability of any MEMS device. This  
163 prototype will enable the development of a new density contrast imaging technology applicable  
164 in many industrial, defence, civil, and environmental applications. It has the potential to be

165 inexpensive, mass-produced and lightweight which opens up new markets: it could be flown in  
166 drones by oil and gas exploration companies, limiting the need for dangerous low altitude aeroplane  
167 flights; it could be used to locate subterranean tunnels; it could be used by building contractors to  
168 find underground utilities. Networks of sensors could be operated in unsafe areas for monitoring  
169 natural and man-made hazards; for example, on volcanoes or unstable slopes to improve the spatial  
170 and temporal resolution of subsurface density changes. This will allow improved hazard forecasting  
171 and the reduction of occupational risk to monitoring personnel<sup>25, 29</sup>.

## 172 **References**

- 173 [1] Van Camp, M. Uncertainty of absolute gravity measurements. *J. Geophys. Res: Solid Earth*  
174 **110**, B05406 (2005).
- 175 [2] Jiang, Z. *et al.* Relative gravity measurement campaign during the 8th international compar-  
176 ison of absolute gravimeters (2009). *Metrologia* **49**, 95–107 (2012).
- 177 [3] Lederer, M. Accuracy of the relative gravity measurement. *Acta Geodyn. Geomater.* **6**, 383–  
178 390 (2009).
- 179 [4] Goodkind, J. M. The superconducting gravimeter. *Revi. Sci. Instrum.* **70**, 4131–4152 (1999).
- 180 [5] de Angelis, M. *et al.* Precision gravimetry with atomic sensors. *Meas. Sci. and Technol.* **20**,  
181 022001 (2008).
- 182 [6] Farrell, W. E. Earth tides, ocean tides and tidal loading. *Philos. T. Roy. Soci. A* **274**, 253–259  
183 (1973).
- 184 [7] D’Alessandro, A. & D’Anna, G. Suitability of low-cost three-axis MEMS accelerometers in  
185 strong-motion seismology: tests on the LIS331DLH (iPhone) accelerometer. *B. Seismol. Soc.*  
186 *Am.* **103**, 2906–2913 (2013).
- 187 [8] Krishnamoorthy, U. *et al.* In-plane MEMS-based nano-g accelerometer with sub-wavelength  
188 optical resonant sensor. *Sensor. Actuat. A-Phys* **145-146**, 283–290 (2008).
- 189 [9] Lainé, J. & Mougénot, D. A high-sensitivity MEMS-based accelerometer. *The Leading Edge*  
190 **33**, 1234–1242 (2014).
- 191 [10] Pike, W. T., Delahunty, A. K., Mukherjee, A. & Standley, I. M. A self-levelling nano-g silicon  
192 seismometer. In *Proc. IEEE Sensors 2014*, 1599 – 1602 (IEEE, Valencia, 2014).

- 193 [11] Bertolini, A., Cella, G., Desalvo, R. & Sannibale, V. Seismic noise filters , vertical resonance  
194 frequency reduction with geometric anti-springs : a feasibility study. *Nucl. Instrum. Meth. A*  
195 **435**, 475–483 (1999).
- 196 [12] Cella, G. *et al.* Seismic attenuation performance of the first prototype of a geometric anti-  
197 spring filter. *Nucl. Instrum. Meth. A* **487**, 652–660 (2002).
- 198 [13] Pike, W. T., Standley, I. M. & Calcutt, S. A Silicon Microseismometer For Mars. In *Trans-*  
199 *ducers and Eurosensors XXVII*, 622–625 (2013).
- 200 [14] Carbone, L. *et al.* Sensors and actuators for the Advanced LIGO mirror suspensions. *Classical*  
201 *Quant. Grav.* **29**, 115005 (2012).
- 202 [15] Bell, C. J., Reid, S. & Faller, J. Experimental results for nulling the effective thermal expansion  
203 coefficient of fused silica fibres under a static stress. *Classical Quant. Grav.* **31**, 065010 (2014).
- 204 [16] Hull, R. *Properties of Crystalline Silicon* (Institution of Engineering and Technology, London,  
205 1999), 1st edn.
- 206 [17] Poggi, M. A., McFarland, A. W., Colton, J. S. & Bottomley, L. A. A method for calculating  
207 the spring constant of atomic force microscopy cantilevers with a nonrectangular cross section.  
208 *Anal. Chem.* **77**, 1192–1195 (2005).
- 209 [18] Cho, C. H. Characterization of Young’s modulus of silicon versus temperature using a “beam  
210 deflection” method with a four-point bending fixture. *Curr. App. Phys.* **9**, 538–545 (2009).
- 211 [19] Van Camp, M. & Vauterin, P. Tsoft: graphical and interactive software for the analysis of  
212 time series and Earth tides. *Comput. Geosci.* **31**, 631–640 (2005).

- 213 [20] Callen, H. B. & Welton, T. A. Irreversibility and Generalized Noise. *Phys. Rev.* **83**, 34–40  
214 (1951).
- 215 [21] Chin, E., Lee, K., Winterflood, J., Ju, L. & Blair, D. Low frequency vertical geometric  
216 anti-spring vibration isolators. *Phys. Lett. A* **336**, 97–105 (2005).
- 217 [22] Aparicio, S. S.-M., Sampedro, J. A., Montesinos, F. G. & Molist, J. M. Volcanic signatures in  
218 time gravity variations during the volcanic unrest on El Hierro (Canary Islands). *J. Geophys.*  
219 *Res: Solid Earth* **119**, 5033–5051 (2014).
- 220 [23] Mogi, K. Relations between the eruptions of various volcanoes and the deformations of the  
221 ground surfaces around them. *B. Earthq. Res. I.* **36**, 99–134 (1958).
- 222 [24] Battaglia, M., Gottsmann, J., Carbone, D. & Fernandez, J. 4D volcano gravimetry. *Geo-*  
223 *physics* **73**, WA3–WA18 (2008).
- 224 [25] Rymer, H., Williams-Jones, G. & Keynes, M. Gravity and deformation measurements. *Geo-*  
225 *phys. Res. Lett.* **27**, 2389–2392 (2000).
- 226 [26] Allan, D. Statistics of atomic frequency standards. *Proc. IEEE* **54**, 221–230 (1966).
- 227 [27] Peterson, J. Observations and modeling of seismic background noise. *U.S. Geological Survey.*  
228 *Open-File Report* 93–322 (1993).
- 229 [28] Essen, H. H., Kruger, F., Dahm, T. & Grevemeyer, I. On the generation of secondary micro-  
230 seisms observed in northern and central Europe. *J. Geophys. Res: Solid Earth* **108**, 2506–2520  
231 (2003).
- 232 [29] Baxter, P. J. & Gresham, A. Deaths and injuries in the eruption of Galeras volcano, Colombia,  
233 14 January 1993. *J. Volcanol. Geoth. Res.* **77**, 325–338 (1997).

234 [30] Riccardi, U., Rosat, S. & Hinderer, J. Comparison of the Micro-g LaCoste gPhone-054 spring  
235 gravimeter and the GWR-C026 superconducting gravimeter in Strasbourg (France) using a  
236 300-day time series. *Metrologia* **48**, 28–39 (2011).

## 237 Print figure legends

- 238 • **Figure 1: The MEMS Device.** A figure demonstrating the design of the MEMS gravime-  
239 ter. The central proof mass is suspended from three flexures: an anti-spring pair at the  
240 bottom and a curved cantilever at the top. The anti-spring pair constrain the motion of the  
241 proof mass along the red axis. The frequency is lowered by this constraint until the cantilever  
242 pushes the motion off-axis, stabilising the MEMS device at a lower frequency.
- 243 • **Figure 2: The Experimental Set-up.** A schematic of the MEMS device and the shadow  
244 sensor. Both sit on an aluminium plate and are encased in a copper thermal shield. Both  
245 the MEMS device and the shield are thermally controlled. At the top left is a photograph  
246 and scanning electron microscope (SEM) image of the MEMS device. At the bottom left is  
247 a photograph of the MEMS device mounted on the optical shadow sensor with glue holding  
248 the heater and thermometer in place.
- 249 • **Figure 3: The Earth Tides.** The measurements of the Earth tides obtained from the  
250 MEMS device. The data has been averaged with a time constant of 240 minutes. The red  
251 line is a theoretical plot calculated with *TSOFT*, including an ocean loading correction. The  
252 blue line is the experimental data. The two series have a correlation coefficient of 0.86.
- 253 • **Figure 4: Drift Characteristics.** **4a** is a full noise time series of the tide measurement. **4b**  
254 is the Allan Deviation of the series in **4a**. **4c** is a full noise time series of the tide measurement  
255 with the tide signal removed via a regression against the theoretical data from *TSOFT*. **4d**  
256 is the Allan Deviation of the series in **4c**. **4e** is a time series of the tide measurement with  
257 the tides removed and the linear drift corrected, **4f** is the corresponding Allan deviation plot.  
258 **4g** is the same data as **4e** but with a 4 hour filter added. **4h** is the Allan deviation plot of



259 this filtered data.

## 260 **Extended data figure legends**

- 261 • **Figure 5: Spring Resonant Frequency Behaviour with Tilt** The resonant frequency  
262 decreases as the MEMS device gets closer to vertical due to the geometrical anti-spring effect.  
263 At  $88^\circ$  and  $92^\circ$  there are minima in the plot. At this point the frequency is constant  
264 with tilt and the system displays a Hooke's law behaviour. The resonant frequency of a  
265 symmetric anti-spring would reach an instability here. This figure also demonstrates that  
266 whilst the instrument is operated at  $90^\circ$  the resonant frequency is 2.3 Hz, it can be lowered  
267 to 1.8 - 1.9 Hz by tilting to operate to one of the minima.
  
- 268 • **Figure 6: The Earth Tides with Different Filtering.** Figure 6a presents measurements  
269 of the Earth tides obtained from the MEMS device. This is the raw data output. Figure  
270 6b presents the same data but with a 10 minute filtering time. The red lines are theoretical  
271 plots calculated by *TSOFT*. The blue lines are the experimental data.
  
- 272 • **Figure 7: Quality Factor Frequency Dependence.** We observe a trend of decreasing  
273 quality factor with decreasing frequency of our device. At low frequencies the internal friction  
274 of the material becomes the dominant loss mechanism. This trend has been discussed by  
275 Chin et al.<sup>21</sup>.
  
- 276 • **Figure 8: Geometrical Anti-Spring Design.** Figures 8a and 8b demonstrate the  
277 Hooke's-law behaviour of a straight and curved cantilever respectively. Figures 8c and 8d  
278 demonstrate the unstable anti-spring characteristics of a 2 and 4 flexure MEMS device re-  
279 spectively. Figure 8e demonstrates behaviour of a 3 flexure MEMS device (see figure 1).

280 Whilst a 2 or 4 flexure system reaches an instability with increasing load, a 3 flexure system  
281 regains a Hooke's law behaviour. The 3-flexure system behaves as such because it is pushed  
282 off its constrained axis by the asymmetry of the design. All of these plots were produced  
283 using *Ansys* finite element analysis software.

284 • **Figure 9: Polynomial Drift.** This plot demonstrates the drift in the data shortly after the  
285 vacuum pump has been turned on. A polynomial component to the drift is clearly visible.  
286 Once the vacuum system has settled, however, the drift becomes linear as demonstrated in  
287 figure 4b at a level of  $150 \mu\text{Gal}/\text{day}$ .

288 • **Figure 10: MEMS Device RMS Acceleration Sensitivity.** Figure 10a demonstrates  
289 the RMS acceleration sensitivity in  $\mu\text{Gal}$ , and figure 10b in  $\mu\text{Gal-dB}$ . The tide signal can be  
290 observed in both plots at  $10^{-5}$  Hz; the peak at  $2 \times 10^{-3}$  Hz is the artefact of the temperature  
291 servo discussed earlier; the microseismic peak can be observed 0.1 Hz and 0.2 Hz; and the  
292 2.3 Hz resonant frequency can be observed to the right of the plot. The plot is a composite  
293 of two data series because the temporal resolution required to record the higher frequency  
294 data would not be possible to maintain at lower frequencies.

295 • **Figure 11: Power Spectral Density Comparison.** The red series – plotted using the  
296 data from 4g – is our MEMS device, demonstrating its sensitivity in the tidal frequency range.  
297 The filtering time means that the sensitivity rolls off above  $10^{-4}$  Hz. The black series is the  
298 *Scintrex CG5*, the blue series is the *Micro-g Lacoste gPhone-054*, the green series is the *SG-*  
299 *C026 superconducting gravimeter*. The data from these three series are taken from a figure by  
300 Riccardi et. al.<sup>30</sup> (©Bureau International des Poids et Mesures. Reproduced by permission  
301 of IOP Publishing. All rights reserved.). The magenta series is the microseismometer by  
302 Pike et. al. (private communication by permission of the author, to be published in the 47th

303 Lunar and Planetary Science Conference).

304 • **Figure 12: Tilt Susceptibility Tests.** Figure **12a** demonstrates the variation in output  
305 of the MEMS device with the x-axis tilt of the sensor plotted on a secondary axis. Figure  
306 **12b** shows the same for the y-axis. There is a x-axis (in-plane MEMS tilt) a tilt sensitivity  
307 in this axis of  $21.2 \mu\text{Gal}/\text{arc second}$ , but in the x-axis (out of plane MEMS tilt) the tilt  
308 sensitivity of only  $0.6 \mu\text{Gal}/\text{arc second}$ .

309 • **Figure 13: Long Term Reproducibility Tests.** Figures **13a** and **13b** are two data sets  
310 separated by approximately 4 months, with no filtering employed. During this period the  
311 vacuum chamber was evacuated and vented several times, despite this the calibration factor  
312 of the device has not changed by more than 5%.

## 313 **Methods**

### 314 **MEMS device fabrication**

315 The MEMS device was fabricated from a single chip of 200  $\mu\text{m}$  thick silicon. The reverse side of  
316 the wafer was first coated with 2.5  $\mu\text{m}$  of PECVD  $\text{SiO}_2$ . A 100 nm coating of chromium was next  
317 deposited on the top surface of the silicon using a thermal evaporator.

318 The MEMS device pattern was created in a layer of positive photoresist using a g-line pho-  
319 tolithography process. The mask was a ‘halo’ design<sup>31</sup> i.e. instead of etching away all of the  
320 unwanted areas of silicon, trenches were used in an outline of the structure, to keep a constant  
321 etch rate and profile over all etched areas. The halo was 10  $\mu\text{m}$  wide. The photoresist pattern  
322 was then used as a mask to wet etch the chrome using a nitric acid chrome etchant for 100 s,  
323 thus etching the MEMS device proof mass pattern into the chrome. The resist was then removed  
324 ultrasonically with acetone and isopropanol, leaving the chrome etch mask in place. A 7  $\mu\text{m}$  layer  
325 of AZ<sup>®</sup>-4562 photoresist was then spun onto the back of the sample and used later in making the  
326 sample free standing.

327 The sample was fixed to a carrier wafer (chrome side up) using a thin, spun-on layer of  
328 *Crystalbond*<sup>®</sup> 509 in solution with acetone. To ensure a good thermal contact the sample was  
329 weighted and left on the hotplate at 88° C (just above the melting point of *Crystalbond*<sup>®</sup>) for  
330 5 minutes. The sample was next placed in an *Oxford Instruments PlasmaPro 100 Estrelas Deep*  
331 *Silicon Etch System*, and Bosch<sup>™</sup> etched<sup>32</sup> for 80 minutes using an  $\text{SF}_6$ ,  $\text{C}_4\text{F}_8$  process optimised  
332 for highly anisotropic trenches. This etch was the same depth as the silicon and stopped when it  
333 reached the  $\text{SiO}_2$  back layer. The *PlasmaPro 100 Estrelas Deep Silicon Etch System* allows control  
334 of the gas flow enabling processes to be tuned with negative and positive defined etch profiles. Our  
335 spring profiles are vertical to within 0.5°.

336 To remove the sample from the carrier wafer it was heated to 88° C for 5 minutes, and then  
337 pushed laterally off the - now fluid - *Crystalbond*<sup>®</sup>. The SiO<sub>2</sub> and AZ<sup>®</sup>-4562 layers enabled this to  
338 be done without damaging the MEMS device structure. The sample was then turned upside down  
339 and placed (not affixed) to a blank piece of silicon. The residual *Crystalbond*<sup>®</sup> and photoresist  
340 were removed from the bottom of the sample using an O<sub>2</sub> plasma ash. The sample was exposed  
341 to a CF<sub>4</sub>/O<sub>2</sub> etchant plasma until all of the SiO<sub>2</sub> was removed, making the sample free standing.

## 342 Geometrical Anti-Spring Design

343 Our MEMS device is comprised of a proof mass, suspended from three curved cantilevers/flexures.  
344 To better understand the physical characteristics of this system we first discuss these flexures  
345 individually. Consider a cantilever, clamped at one end, and free to move at the other. A proof  
346 mass mounted on the moving end will oscillate with a frequency that depends on the geometry  
347 of the cantilever, and the Young's modulus of the material from which it is made. The proof  
348 mass will oscillate along an arc, defined by the length of the flexure. The system will behave as  
349 a Hooke's law spring, with a linear relationship between force and displacement. This behaviour  
350 can be observed in figure 8a. A curved single cantilever also behaves in the same manner, as seen  
351 in figure 8b.

352 To create an anti-spring, one can take two such curved cantilevers and attach them at a central  
353 pivot point. A proof mass mounted at this point will no longer be able to trace out an arc as it  
354 oscillates. Instead – because of the symmetrical forces applied by the two identical cantilevers – its  
355 motion will be constrained along a vertical axis (as presented in figure 1). It is this constraint that  
356 forces the spring constant to change as the displacement increases. Instead of observing a linear  
357 relationship between force and displacement, a non-linear behaviour is found. This behaviour can  
358 be observed in figure 8c. This now means that the spring gets softer with increasing displacement.

359 A four flexure anti-spring system is a simple extension of a two-flexure system. Here, a second  
360 pair of cantilevers are placed below the first pair, this allows a non-point source proof mass to  
361 be suspended. The behaviour of the spring is still non-linear, and is displayed in figure 8d. The  
362 behaviour is identical to that of a two flexure system, except the system can support twice the  
363 mass.

364 Both the two and four anti-spring systems can be used to create oscillators that have low  
365 resonant frequencies. When the limits of  $k/m$  are pushed to create the lowest resonant frequency  
366 possible, however, these systems become unstable. They become unstable because the motion is  
367 so well constrained along its vertical axis, the spring gets softer and softer until it can no longer  
368 support the weight of the proof mass. This behaviour can be observed in figures 8c and 8d: as the  
369 force increases, the displacement increases rapidly. A stable resonant frequency is imperative for  
370 a useful relative gravimeter, therefore this instability would create problems if used for the design  
371 of a MEMS gravimeter. It would require the use of a closed-loop feedback system.

372 Our MEMS device utilises a novel three-flexure anti-spring system, with one flexure of the upper  
373 pair of cantilevers removed (see figure 1). In the first instance, the device behaves as a four-flexure  
374 anti-spring: it gets rapidly softer as the displacement of the proof mass increases. The anti-spring  
375 behaviour is maintained while the proof mass moves along its vertically constrained axis. The  
376 asymmetry of the system, however, means that the device does not stay constrained along the  
377 anti-spring constraining axis. The single upper flexure ultimately tilts the proof mass marginally  
378 away from the constraining axis. As the motion is pulled from this axis, the anti-spring trend is  
379 halted and the device regains a Hooke's law behaviour, where  $dF/dz = constant$ . This behaviour  
380 can be observed in figure 8e where the gradient of force vs displacement reaches a minimum at  
381  $z = 0.6$ . This means that the device assumes a constant spring constant at the maximum stiffness  
382 value that we have demonstrated to be stable over many months (as demonstrated by figure 13).

## 383 **Optical shadow sensor**

384 The proof mass motion is measured using an optical shadow sensor<sup>14</sup>. Using a fused silica ‘C’-  
385 shaped support structure, a red LED (powered at 0.3 mW) was shone onto a split photodiode,  
386 with the MEMS device proof mass mounted in between. The change in intensity incident on the  
387 photodiode resulting from the motion of the proof mass shadow was then used as a measure of the  
388 motion. The split photodiode was made from two 5 mm by 10 mm planar silicon photodiodes, and  
389 wired to give a differential output. A split photodiode was used so that at the nominal position of  
390 the proof mass the output signal was zero. This allowed maximal amplification without saturation  
391 of the measurement instrumentation. The LED signal was modulated (at a frequency of 107 Hz  
392 with a 50:50 duty cycle) to reduce the 1/f noise in the output signal. The modulation was carried  
393 out by turning the LED on and off with an *HP 33120A* square wave signal generator. A precision  
394 current stabilising resistor (displayed in figure 2 maintained the LED drive current, this was heat  
395 sunk to the fused silica ‘C’-shaped structure. The current output from the photodiode was first  
396 converted into a voltage using an *SRS SR570* current-to-voltage converter, band-passed between  
397 3 Hz to 100 Hz, and amplified by a factor of  $10^6$  V/A. This amplified signal was then de-modulated  
398 via an analogue lock-in amplifier (*Femto LIA-MV-200*) referenced from the signal generator. The  
399 lock-in amplified the signal with a gain of 10 and undertook readings with a time constant of  
400 3 s. This analogue signal was passed through an *SRS SR560* low pass filter 0.03 Hz to remove  
401 aliasing and filter seismic noise, before being digitised via a 16 bit, 12 dB/octave, analogue-to-  
402 digital converter (*National Instruments M Series 6229*) and recorded by a computer with a 24 s  
403 time constant. Analogue signals were used to reduce digitisation noise that would have occurred  
404 if a digital signal had been amplified by this magnitude.

405 The shadow sensor has a readout noise floor of  $\leq 10 \mu Gal$  at the sampling frequency of 0.03 Hz,

406 and a dynamic range of  $\sim 50 \mu m$ . A large dynamic range is required because of the large initial  
407 displacement (0.8 mm) of the proof mass when it is tilted to its vertical operating orientation,  
408 thus making initial alignment of the MEMS device difficult. Although the maximum peak-to-peak  
409 displacement of the proof mass caused by the tides is only 16 nm, the proof mass also oscillates  
410 at its resonant frequency by up to 100 nm due to seismic ground motion. A high dynamic range  
411 is also useful to measure this signal, which is ultimately removed from the data by averaging with  
412 a 0.03 Hz filter in the readout electronics.

## 413 **Temperature control**

414 The control loops used to maintain the temperature of the system were proportional integral  
415 derivative (PID) control mechanisms, written in *Labview*. Temperatures were monitored using a  
416 four-terminal measurement of small platinum resistors, via two *Keithley 2000* digital multimeters.  
417 A four-terminal measurement eradicates contact resistance by driving the thermometer with a  
418 current and measuring the voltage across it. This removes the temperature sensitivity of external  
419 wires. Low temperature coefficient *Manganin*<sup>®</sup> wires were used for these connections to minimise  
420 parasitic thermal conduction. One platinum resistor was placed on the outer frame of the MEMS  
421 device and three were placed equidistantly around the copper shield. Wire wound resistors were  
422 used as the heating mechanism to feedback into the system; again, one of these was placed on  
423 the MEMS device frame and three around the shield. The output signal to the heaters was sent  
424 via a *National Instruments (USB 6211)* card, and the heaters were powered with non-inverting  
425 amplifiers with a capability to power up to 100 mA. All circuitry and instrumentation used to  
426 amplify and measure the output signal, and to measure and control the system temperature, were  
427 selected for their high thermal stability. This entire configuration was constructed in a vacuum  
428 chamber with a pressure of  $\leq 10^{-5}$  mTorr.



## 429 Data analysis

430 Although PID control was implemented for the MEMS device and the shield, there were other  
431 components with variations that could not be actively controlled. Namely the room temperature  
432 that coupled into the data via a temperature sensitive lock-in amplifier, and intensity variations of  
433 the LED that were monitored using a monitor photodiode. There was also an offset, and a linear  
434 drift of under  $150 \mu\text{Gal}$  per day once the system had been left evacuated for over a week. This drift  
435 term is due to stress in the silicon flexures. Like all mechanical systems, application of stress leads  
436 to anelasticity which causes creep and drift over long timescales. Our device also shows polynomial  
437 drift which decays away approximately one week after evacuating the apparatus. The polynomial  
438 drift is likely due to adsorbed water on the surface layer of silicon, and could be mitigated against  
439 by baking out the system before evacuation. Figure 9 demonstrates this initial polynomial drift.  
440 The data were therefore regressed against the temperature measurements listed above, the drift  
441 offset and the intensity. This regression – carried out in *Matlab* with the *mregg* tool – identified  
442 correlations between the output data and these parameters, and removed any resulting correlated  
443 trends from the final data. Floor tilt and power variation of the LED were also monitored, but  
444 neither had any discernable effect on the signal and were therefore not regressed.

445 The correlation coefficient,  $R$ , between the averaged theoretical and experimental tide data  
446 was calculated using *Matlab*'s '*corrcoeff*' function. An  $R$  value of 0.86 was produced, for the plot  
447 presented in figure 3. To check the level of significance of our experimental data we compared it  
448 to the correlation of the noise alone. We created 10,000 random permutations of our data set and  
449 calculated the correlation coefficient for each with respect to the theoretical data. This set of  $R$   
450 values were plotted as a histogram. This histogram had a distribution with a mean value of zero  
451 and a standard deviation of 0.008. The  $R$  value from the un-randomised data is  $114 \sigma$  from this

452 distribution suggesting the correlation is real to an extremely high degree of confidence.

453 Figure 10 is a plot of the RMS acceleration sensitivity of the device over its full spectral  
454 range. The tide signal can be observed at  $1 \times 10^{-5}$  Hz. The peak at  $10^{-3}$  Hz is an artefact of  
455 the temperature servo. Between 0.1 Hz and 0.2 Hz the micro-seismic peak can be recognised,  
456 its presence indicates that the device is also a sensitive seismometer. Past observations – made  
457 from Scotland in February to March 2000 – of the microseismic peak<sup>28</sup> confirm the validity of  
458 our observation. At 2.3 Hz the primary resonant mode of the MEMS device generates a large  
459 peak due to excitation from seismic noise. This plot was used to calculate the sensitivity of the  
460 MEMS device. To find a sensitivity in  $\mu\text{Gal}/\sqrt{\text{Hz}}$ , it is just necessary to read off the acceleration  
461 sensitivity at the point where the data crosses 1 Hz on the horizontal axis. We believe that the  
462 value of  $40 \mu\text{Gal}/\sqrt{\text{Hz}}$  is an overestimate of the true sensitivity of the device because at 1 Hz the  
463 influence of both the primary resonance of the device and the micro-seismic peak are significant.

## 464 **Tilt variation**

465 Although tilt did not have an effect on the tide measurement, we are interested to know at what  
466 point tilt would become an issue. Figure 12 presents two plots of an experiment used to asses the  
467 effect of tilt on our device. Inside the vacuum tank, the MEMS device was mounted vertically and  
468 aligned with the tilt sensor. The y-axis of the tilt sensor was aligned with the plane of the MEMS  
469 device, with the x-axis perpendicular to this (see Fig. 1). Figure 12a demonstrates the induced  
470 tilts of the tank in both x and y axes in arc seconds. Figure 12b demonstrates the corresponding  
471 change in the output of of the device in  $\mu\text{Gal}$ . There is a strong correlation between the y axis  
472 variation and the voltage output, giving a tilt sensitivity in this axis of  $21.2 \mu\text{Gal}/\text{arcsec}$ . There  
473 is less sensitivity to the x-axis tilt with a tilt sensitivity of only  $0.6 \mu\text{Gal}/\text{arcsec}$ .

474 The x-axis tilt sensitivity is low because in the vertical configuration, the spring resumes a

475 Hooke's law response as observed in Fig. 5, for which the x-axis tilt variation is plotted against  
476 the resonant frequency (the acceleration sensitivity of the device is proportional to the square of  
477 the resonant frequency). Ultimately the spring could be tuned to operate with even less variation  
478 with tilt in this axis if it were positioned to operate at one of its minima. Alternatively the flexures  
479 could be made marginally thicker to shift the minimum in resonant frequency to  $90^\circ$ , this was not  
480 carried out because the device did not show sufficient tilt sensitivity to cause concern. The y-axis  
481 variation is larger because the device has a mode of oscillation in which the proof mass tilts and  
482 pivots about the upper cantilever flexure.

483 When vertical, the device would need to be levelled with an accuracy limited by the y-axis  
484 sensitivity (i.e. less than 2 arc seconds to maintain the current sensitivity) to make repeatable  
485 measurements in different locations. This accuracy of levelling is achievable with a simple surveyors  
486 bubble level.

## 487 **Temporal Reproducibility Tests**

488 Figure 13 demonstrates two short data sets separated by nearly four months. These were used as a  
489 test of the temporal stability of the device. To convert the raw voltage output of the device into a  
490 unit of acceleration, a calibration factor was required. By comparing the experimental (blue) data  
491 in Fig. 13a with that in 13b we were able to test whether the calibration factor had drifted over  
492 time. The same calibration factor has been used to make both of these plots. By averaging the  
493 data and changing the calibration factor of Fig. 13b, it was found that a change in the calibration  
494 factor of 5% made the fit to the tide theory (red) data noticeably worse. Changes smaller than  
495 this were not possible to resolve. We therefore believe that if the calibration factor has changed,  
496 it has done so by no more than 5%. During this time period, the vacuum tank was vented and  
497 evacuated several times, the MEMS was moved around each time. This is an important feature of

498 a device that could eventually be used in the field.

## 499 **Applications**

500 MEMS gravimeters have significant industrial applications. Given their small size and low cost,  
501 they could be used for down bore-hole exploration in the oil and gas industry<sup>33</sup> and utilised to  
502 monitor well drainage. Such devices could also be utilised for environmental monitoring, where  
503 networks of sensor arrays could monitor sub surface water levels<sup>34</sup>, or to determine the location  
504 of historic landfill sites. The security industry is an area for which low cost/small form factor  
505 gravimeters would also be a transformative technology to detect subterranean tunnels <sup>35,36</sup>, or  
506 imaging of cargo containers where high spatial resolution via numerous sensors is an advantage<sup>37</sup>.  
507 MEMS gravimeters could also be used in civil engineering. At present in many of the UK victorian  
508 cities the placement of utilities is only accurate on maps to within 15 metres of land marks such  
509 as trees, fences or buildings. There have been trials of the *Scintrex CG5* and MEMS based arrays  
510 would offer an exciting opportunity. Gravimetry is already used in volcanology and can be used  
511 to help predict eruptions. Networks of small, low-cost gravimeter arrays could revolutionize the  
512 way volcano gravimetry is carried out<sup>22, 25, 24</sup>.

513 A field prototype is currently being developed at Glasgow that will be the size of a tennis  
514 ball and require a power supply of under 1 W. A powerless getter pump will be used to maintain  
515 vacuum, both the thermal control and the optical readout will be on-chip; tilt levelling will be  
516 included, and all of the read-out and control software will be run on a micro-controller.

## 517 Additional references from methods section

- 518 [31] Pike, W. Analysis of sidewall quality in through-wafer deep reactive-ion etching. *Microelec-*  
519 *tronic Eng.* **73-74**, 340-345 (2004).
- 520 [32] Laermer, F. & Schilp, A. Method of anisotropic etching of silicon. US patent number:  
521 5,501,893 (1996).
- 522 [33] Rim, H. & Li, Y. Advantages of borehole vector gravity in density imaging. *Geophysics.* **80**,  
523 G1-G13 (2015).
- 524 [34] Bauer-gottwein, P., Christiansen, L & Rosbjerg, D. Informing hydrological models with  
525 ground-based time-lapse relative gravimetry : potential and limitations. *GRACE, Remote*  
526 *Sensing and Ground-based Methods in Multi-Scale Hydrology (Proceedings of Symposium J-*  
527 *H01).*, 187-194 (2011).
- 528 [35] Romaides, A. J. et al. A comparison of gravimetric techniques for measuring subsurface void  
529 signals. *J.Phys. D. Appl. Phys.* **34**, 433-443 (2001).
- 530 [36] Butler, D. K. Microgravimetric and gravity gradient techniques for detection of subsurface  
531 cavities. *Geophysics* **49**, 1084-1096 (1984).
- 532 [37] Kirkendall, B., Li, Y. & Oldenburg, D. Imaging cargo containers using gravity gradiometry.  
533 *IEEE Transactions on Geoscience and Remote Sensing* **45**, 1786-1797 (2007).
- 534 [38] Panisova, J. & Pasteka, R. The use of microgravity technique in archaeology: A case study  
535 from the St. Nicolas Church in Pukanec, Slovakia. *Contributions to Geophysics and Geodesy*  
536 **39**, 237-254 (2009).

## 537 **Acknowledgements**

538 The work was funded by the Royal Society Paul Instrument Fund and STFC grant number  
539 ST/M000427/1. The authors would like to thank Dr Matthew Pitkin for advice on complet-  
540 ing significance tests on the data, Dr William Cunningham for advice on finite element modelling,  
541 Mr Michael Perreur-Lloyd and Mr Russell Jones for their help in rendering 3D images of the ap-  
542 paratus, and the staff and other users of the James Watt Nanofabrication Centre for help and  
543 support in undertaking the MEMS fabrication.

## 544 Author contributions

- 545 • R.P.M. led the methodology of the etch process for the MEMS gravimeter and worked with  
546 G.D.H. on the development of the MEMS gravimeter. With G.D.H., he enhanced the long-  
547 term, low-noise stability of the entire system, taking the tide data and performing the com-  
548 putational analysis. He led writing the manuscript.
  
- 549 • A.S. led the methodology of the MEMS mask fabrication. With R.P.M he took the tide  
550 measurements in early 2015 and performed computational analysis of the MEMS gravimeter.
  
- 551 • D.J.P. supervised the design of the MEMS device fabrication process and with G.D.H. came  
552 up with the concept for a MEMS gravity sensor.
  
- 553 • J.H. developed the methodology of utilising geometric anti-springs for the MEMS gravimeter  
554 system and provided critical review/commentary on the manuscript.
  
- 555 • S.R. was responsible for the resources which were necessary to complete the project and  
556 provided critical review/commentary on the manuscript.
  
- 557 • G.D.H. had the initial concept of a MEMS gravimeter together with D.J.P. He had oversight  
558 of the design, fabrication and testing of the gravimeter, via the supervision of R.P.M and A.S.  
559 Together with R.P.M., he characterised and enhanced the low noise performance, resulting  
560 in the measurement of the tides. He was responsible for funding acquisition of the work.

## 561 **Author information**

- 562     • The research data relevant to this letter are stored on the University of Glasgow's Enlighten  
563       Repository, DOI: <http://dx.doi.org/10.5525/gla.researchdata.213>
  
- 564     • Reprints and permissions information is available at [www.nature.com/reprints](http://www.nature.com/reprints)
  
- 565     • The authors have no competing financial interests.
  
- 566     • Correspondence and requests for material should be addressed to [giles.hammond@glasgow.gla.ac.uk](mailto:giles.hammond@glasgow.gla.ac.uk)  
567       or [r.middlemiss.1@research.gla.ac.uk](mailto:r.middlemiss.1@research.gla.ac.uk).





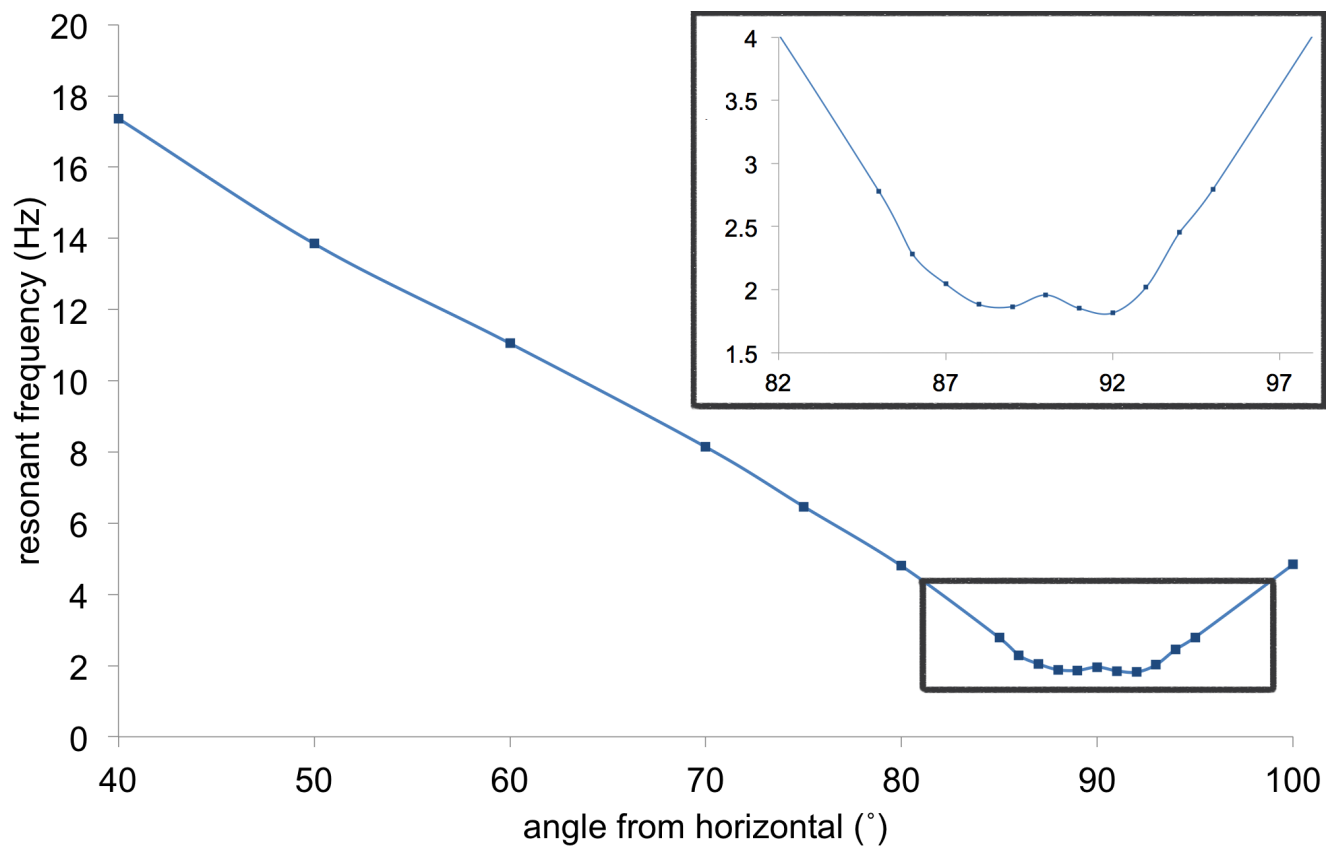
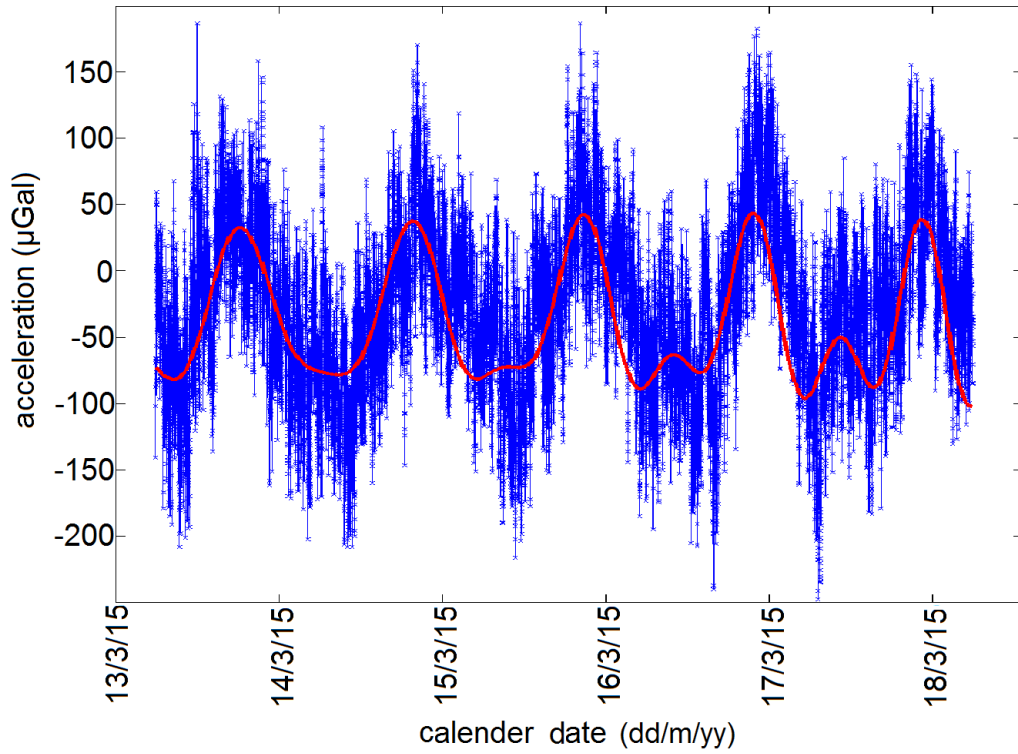
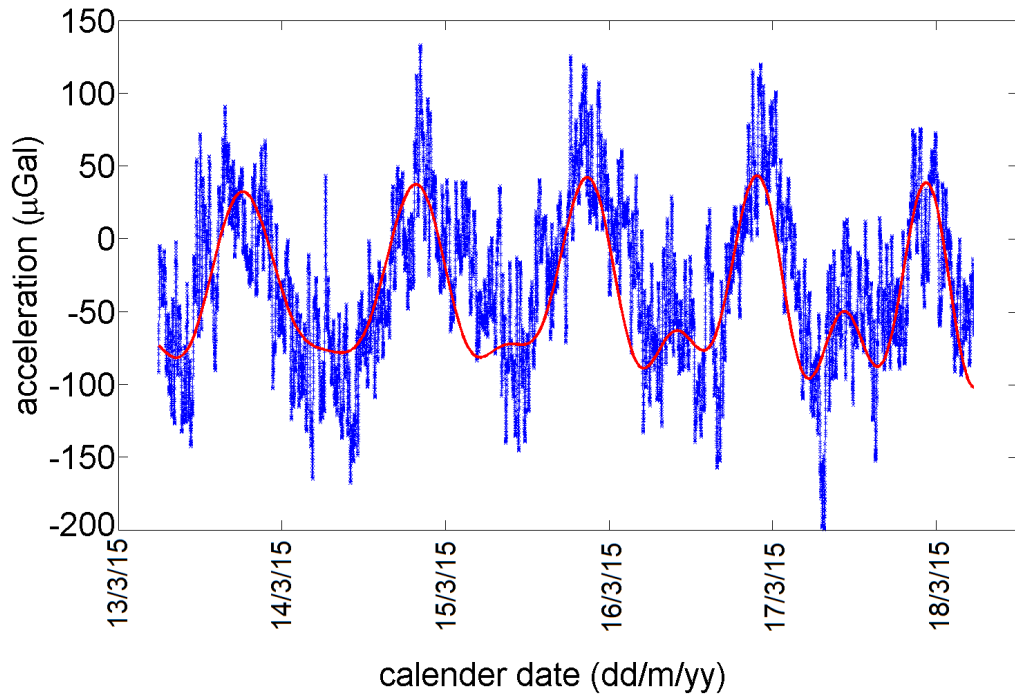


Figure 5



(a)



(b)

Figure 6

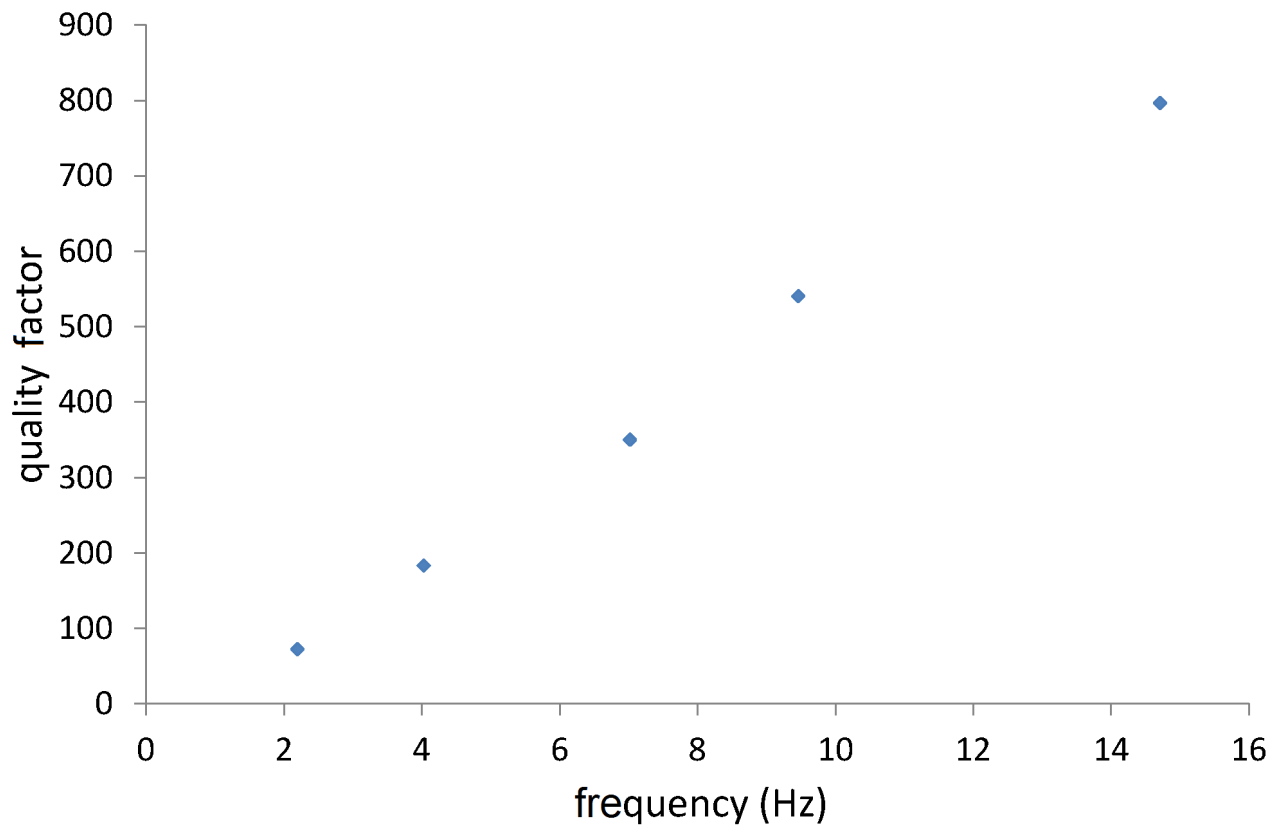
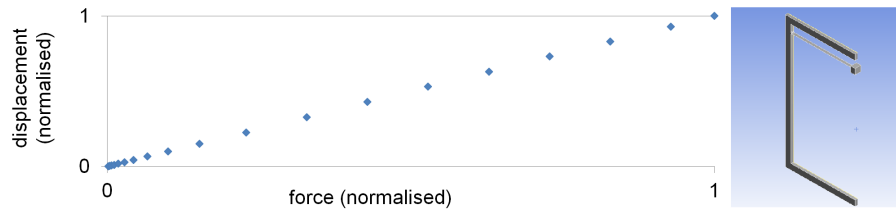
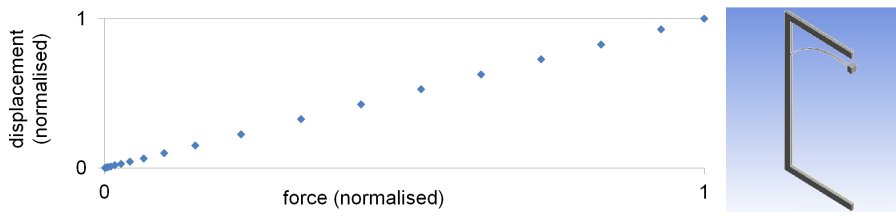


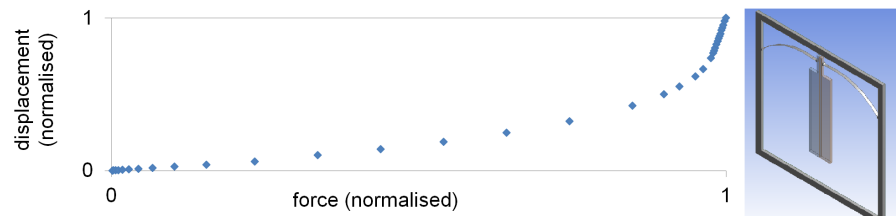
Figure 7



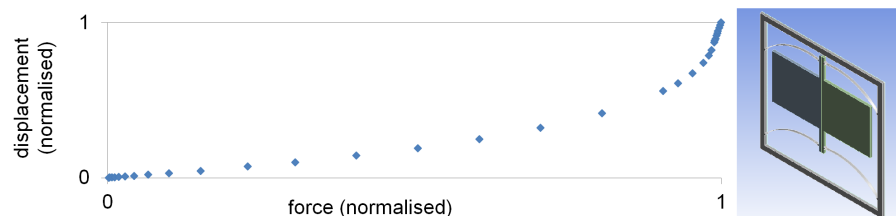
(a)



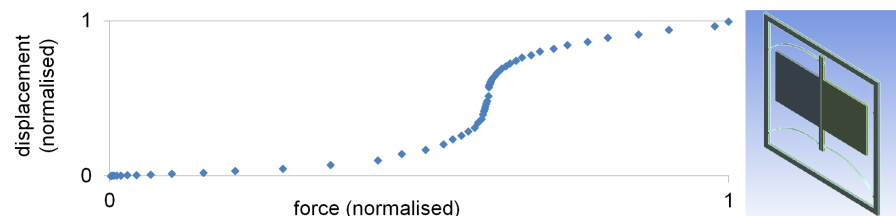
(b)



(c)



(d)



(e)

Figure 8

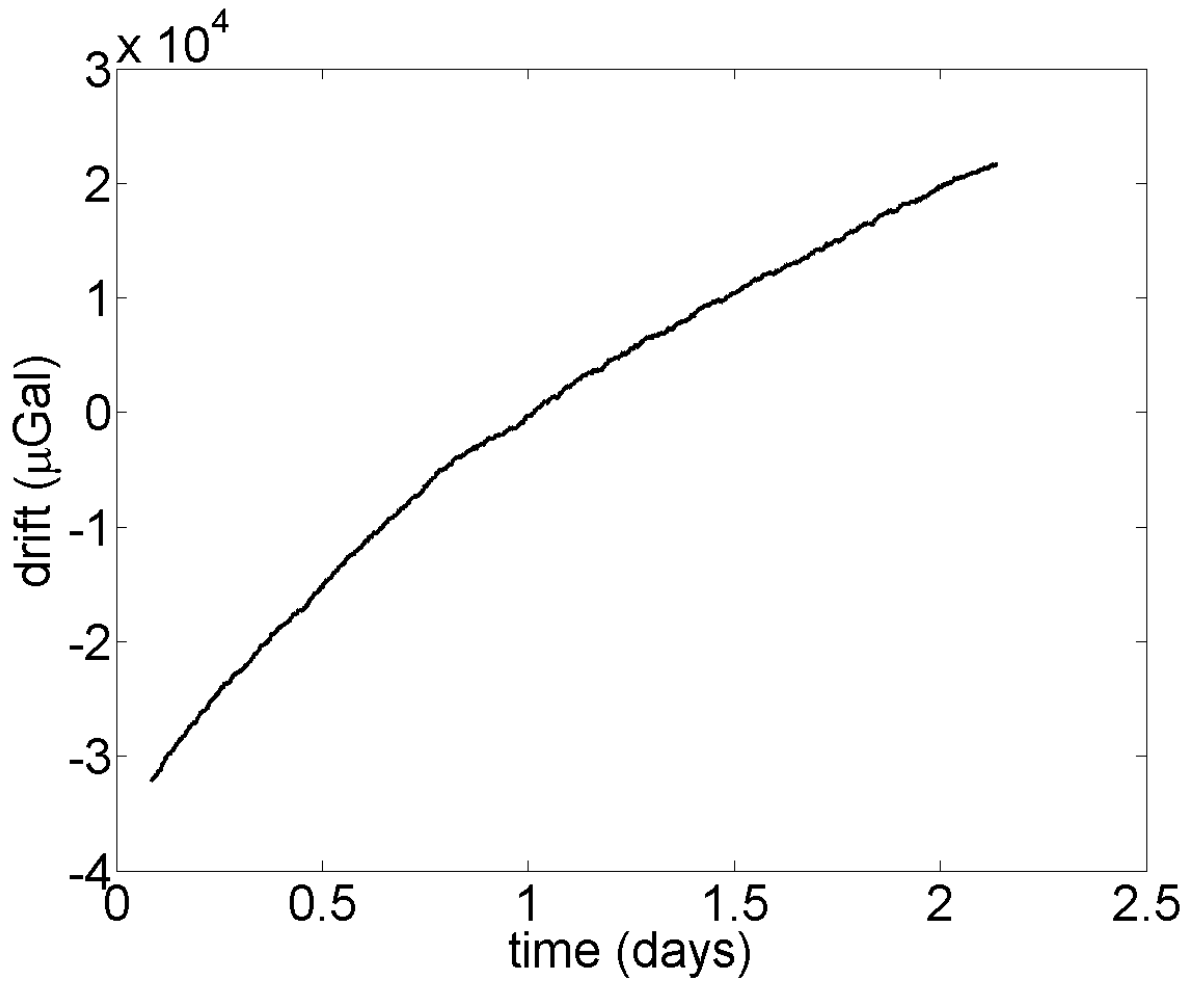
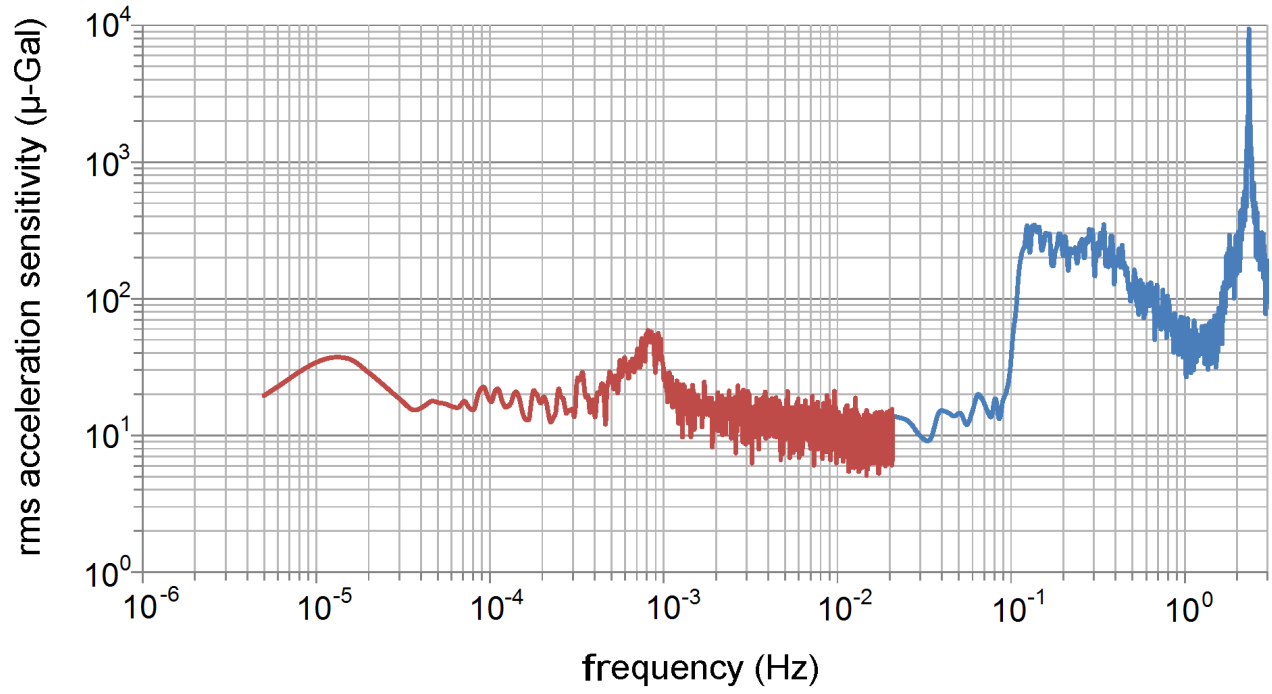
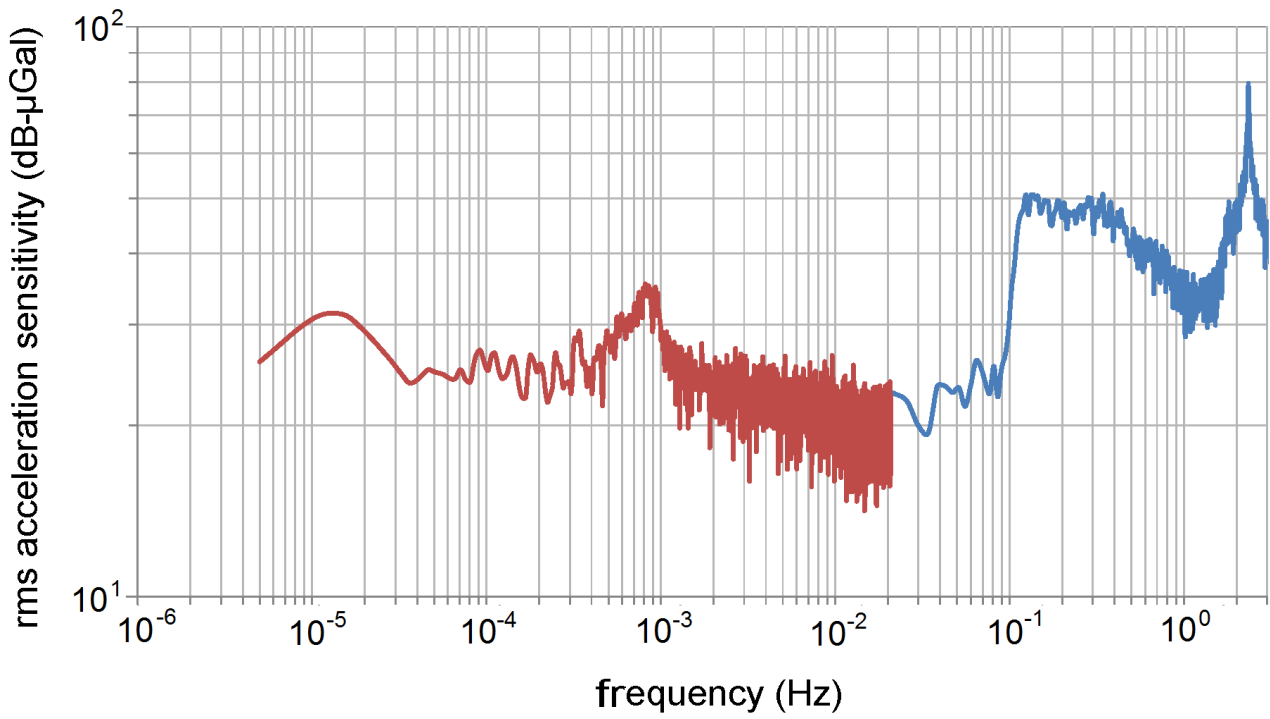


Figure 9



(a)



(b)

Figure 10

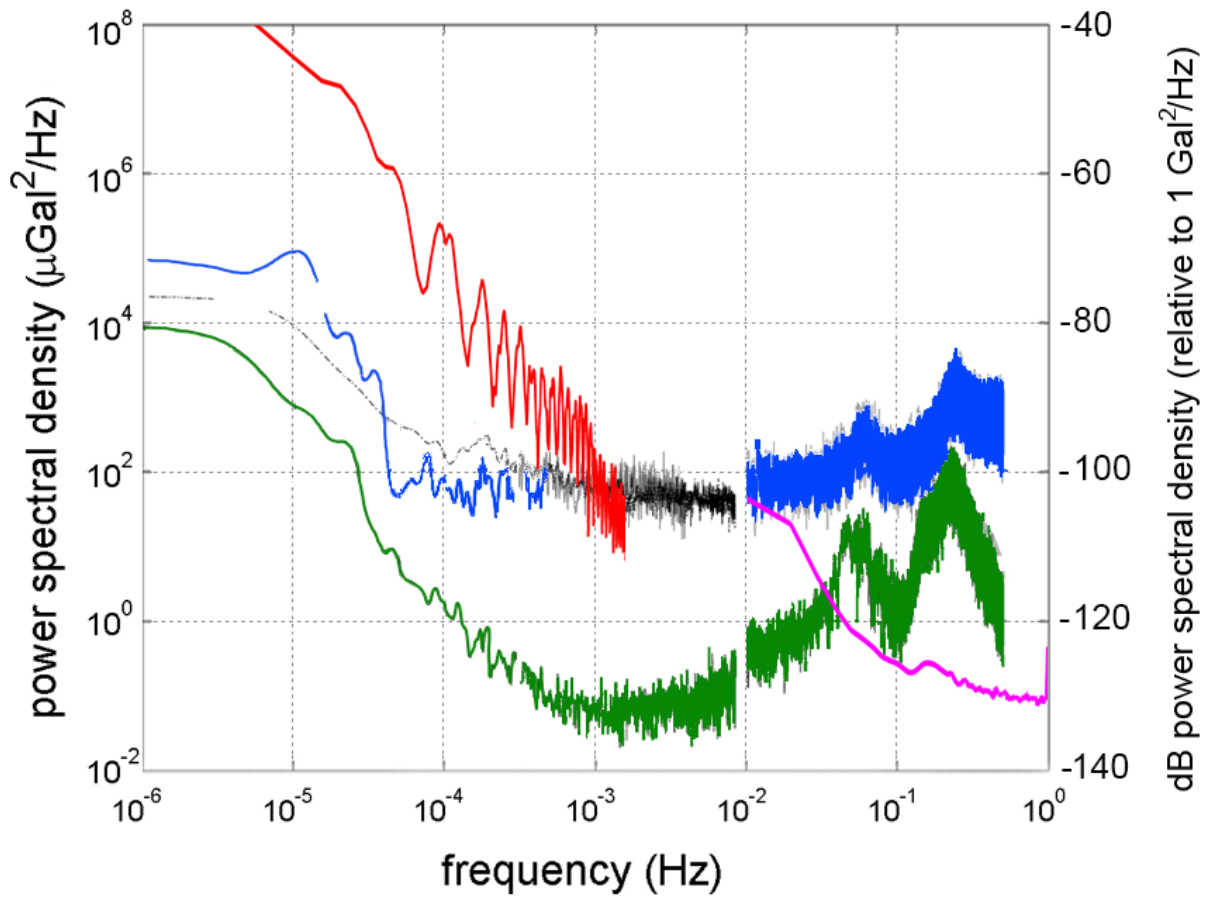
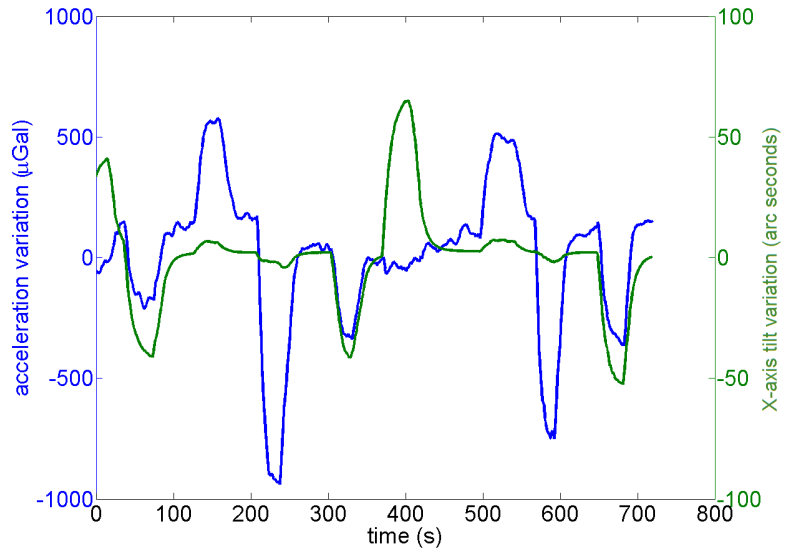
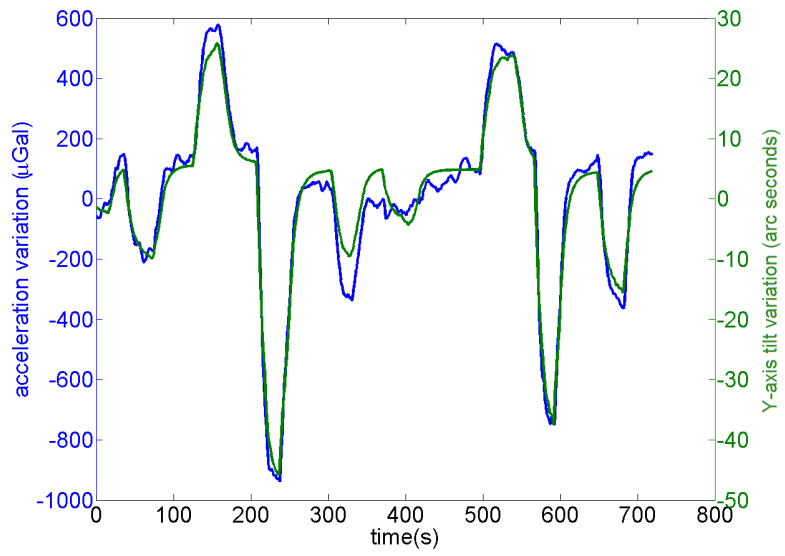


Figure 11



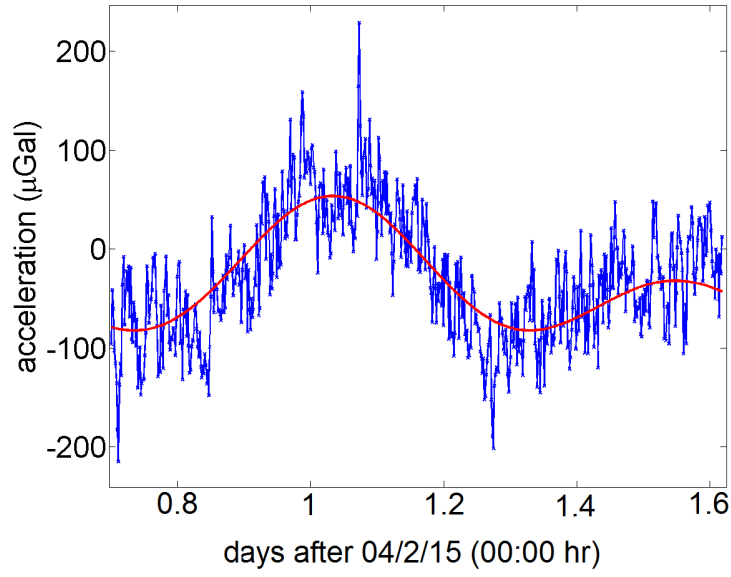


(a)

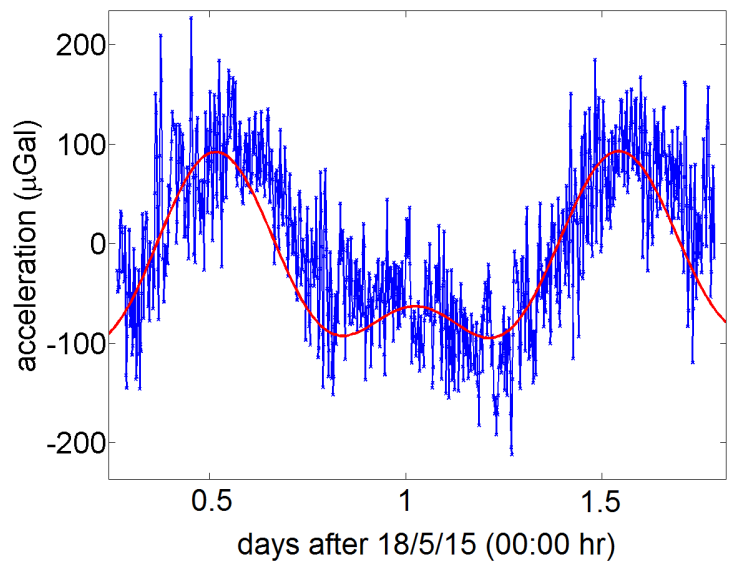


(b)

Figure 12



(a)



(b)

Figure 13

Device	Technology	Sensitivity at 1 Hz	Stability in $\mu\text{Hz}$ Regime	Resonant Frequency	Use
Scintrex CG5 <sup>2,3</sup>	Fused Quartz	2 $\mu\text{Gal}$	0.5 mGal/day	3 Hz	Gravimetry
Krishnamoorthy <sup>8</sup>	MEMS	17 $\mu\text{Gal}$	N/A	36 Hz	Seismology
Quietseis <sup>9</sup>	MEMS	15 $\mu\text{Gal}$	N/A	800 Hz	Seismology
Pike <sup>10</sup>	MEMS	2 $\mu\text{Gal}$	N/A	11 Hz	Seismology
Glasgow MEMS	MEMS	40 $\mu\text{Gal}$	0.14 mGal/day	2.31 Hz	Gravimetry

Table 1: Comparison of Acceleration Sensors